

Superconducting nitridized-aluminum thin films

Alba Torras-Coloma,^{1,2} Leyre Martínez de Olcoz,³ Eva Céspedes,³ Elia Bertoldo,¹
David López-Núñez,^{1,4,5} Sagar Paul,⁶ Wolfgang Wernsdorfer,^{6,7} Gemma Rius,^{3,*} and P. Forn-Díaz^{1,8,†}

¹*Institut de Física d'Altes Energies (IFAE), The Barcelona Institute of Science and Technology (BIST), Bellaterra (Barcelona) 08193, Spain*

²*Departament de Física, Universitat Autònoma de Barcelona, 08193 Bellaterra, Spain*

³*Institute of Microelectronics of Barcelona (IMB-CNM),*

Spanish National Research Council (CSIC), Cerdanyola 08193, Spain

⁴*Barcelona Supercomputing Center, Barcelona 08034, Spain*

⁵*Departament de Física Quàntica i Astrofísica and Institut de Ciències del Cosmos, Universitat de Barcelona, Barcelona 08028, Spain*

⁶*PHI, Karlsruhe Institute of Technology, 76131 Karlsruhe, Germany*

⁷*IQMT, Karlsruhe Institute of Technology, 76344 Eggenstein-Leopoldshafen, Germany*

⁸*Qilimanjaro Quantum Tech SL, Barcelona, Spain*

(Dated: April 9, 2024)

We report the direct observation of superconductivity in nitridized-aluminum thin films. The films are produced by sputtering deposition of aluminum in a controlled mixture of nitrogen diluted in argon. The concentration of applied nitrogen directly determines the properties of the superconducting thin films. We observe samples displaying critical temperatures up to 3.38 ± 0.01 K and resilience to in-plane magnetic fields well above 1 T, with good reproducibility of the results. This work represents an unambiguous demonstration of tunable superconductivity in aluminum-based nitridized thin films. Our results put forward nitridized aluminum as a promising material to be employed in superconducting quantum circuits for quantum technology applications.

I. INTRODUCTION

Superconducting quantum circuits are a leading platform for building applications in quantum technologies, particularly in the field of quantum computation [1, 2]. The performance of these circuits is closely tied to the quality of the materials employed, establishing, e.g., limitations on qubit coherence [3, 4] and on resonator quality [5, 6]. One of the leading loss mechanisms is surface dielectric loss in the form of microscopic two-level defects, ubiquitous in both the substrate-metal and metal-air interfaces of the superconducting quantum devices [7]. Among the strategies to reduce surface dielectric losses, nitrogen-based superconductors, such as NbN, TiN, or NbTiN, have become of great interest in the quantum computing community of superconducting circuits in the last decade, particularly as materials to build resonators and qubit capacitors [8–13]. It is considered that the presence of nitrogen on the surface and within the superconducting thin films helps reducing the impact of two-level system defects that is attributed to native oxides or impurities [14, 15], such as those typically found in aluminum and niobium thin films [16]. In addition, a high degree of disorder is typically attributed to very thin ($\lesssim 20$ nm) nitrogen-based superconductors which explains their characteristic large kinetic inductance [17]. Superconducting thin films with high kinetic inductance are key to produce high-impedance circuits with low losses, a very relevant feature required in high-coherence

superconducting circuits [18] as well as in single photon detectors [19, 20], state-of-the-art parametric amplifiers [21, 22], compact inductance elements and superinductors [23], and kinetic inductance detectors [24, 25].

Motivated by the properties exhibited by nitrogen-based superconductors for quantum circuits, we present here NitrAl (short term for nitridized aluminum), a new superconducting material obtained by depositing aluminum via DC-magnetron sputtering in a controlled atmosphere of nitrogen and argon. To our knowledge, this material has not been analyzed in depth as a superconducting material and only minimal evidence exists on its superconductivity [26, 27].

Crystalline aluminum nitride (AlN) is a well-known wide band-gap material with hexagonal crystal lattice commonly used in microelectronics, for example, as a nanomechanical resonator [28]. In view of its piezoelectric properties it is a suitable candidate for acoustic-wave resonating structures [29]. Recently, AlN has been employed as a bulk acoustic resonator coupled to a superconducting qubit [30]. However, the strong piezoelectricity displayed by AlN results in a loss mechanism through phonon dissipation [28]. Despite this detrimental effect, thin-film dielectric AlN_x has been used as the junction tunnel barrier in both flux [31] and transmon qubits [32], exhibiting long coherence times. The approach followed by both these works consisted on depositing thin films (~ 2 nm) in the cubic phase of AlN which does not display piezoelectricity due to its inversion symmetry. On the other hand, tunnel junctions made of AlN have been sputtered for bolometer applications using an inductively coupled plasma source yielding high quality, highly transparent junctions [33]. These results indicate that the

* gemma.rius@csic.es

† pfordiaz@ifae.es

sources of loss evidenced in wide-bandgap hexagonal AlN can be unimportant in other phases of AlN, existing as e.g. disordered or non-stoichiometric thin films, which may then be used as parts of superconducting circuits.

In contrast to aluminum nitrogen-based superconductors, an oxygen-based superconductor has already been extensively investigated in the form of granular aluminum (grAl) [34]. GrAl consists of aluminum grains embedded in an aluminum oxide matrix and can display superconductivity. Actually, this material presents several properties that make it attractive for a variety of applications, such as in quantum computing circuits [35] or employed in astronomy detectors [36]. GrAl displays a higher critical temperature (T_c) than pure Al, up to 3 K for nitrogen-cooled substrates during deposition [37], and can attain very high room temperature resistivity values, which correlate into superinductor behavior in the superconducting state [38].

Our work presents the unambiguous signatures of superconductivity exhibited by a range of NitrAl thin films produced at different concentrations of applied nitrogen (N_2). We observe the impact of nitrogen concentration on the T_c of the material, as well as the response under large magnetic fields. Our results indicate that NitrAl may be used as a superinductor in quantum circuit applications, as well as in experiments where magnetic field compatibility is desired, such as in semiconductor spin qubits [39] and topological-based condensed matter systems [40].

II. THIN FILM MATERIALS AND METHODS

In this work, we have focused on the dependence of the resulting NitrAl properties as function of the N_2 concentration, while keeping the rest of parameters at a constant value. However, other deposition parameters can significantly influence the properties of the films, such as the working pressure or the power value at the target, which will be considered in future studies.

The Al-based thin films are grown by sputtering technique at the Clean Room of the IMB-CNM-CSIC. The equipment is a DC magnetron sputtering from Karl Suss GmbH, model KS-800 HR. The thin film deposition conditions have been developed for substrates at the 4-inches wafer scale. The substrates consist in commercially-available silicon wafers [41] covered with a high quality insulating silicon dioxide layer, typically 500 nm in thickness deposited also in-house. A wet oxidation technique with a processing temperature of 1100 C was applied for obtaining such a silicon dioxide layer. The metal target is supplied as 99.99% Al, while the processing gases N_2 and Ar are of high purity (> 5.5). The sputtering chamber base pressure is 2×10^{-7} mbar.

The processing parameters for the sputtering deposition, common for all the tests reported in this work, have been established as 60 sccm Ar flow, working pressure $P_w = 5 \times 10^{-3}$ mbar, and power to the target

$P_t = 1000$ W, i.e. those being considered as sputtering conditions within a conventional range. The addition of N_2 is kept in a regime where non-stoichiometric AlN is expected to be obtained, similar to other works using TiN [42]. Specifically, the effect of diluted N_2 in the sputtered Al-based thin film properties and functionality has been tested and fully evaluated for N_2 /Ar fractional flow mainly in the range of 0% to 15%, which correspond to N_2 flow range 0 to 9 sccm (Table I). In this N_2 flow range, the actual deposition rate is determined to be inversely proportional to the applied N_2 flow (Table I), therefore, the corresponding adjustment of the processing time for each N_2 flow value has been applied. A common nominal or target thickness of $t = 100$ nm for the Al and NitrAl thin films is set. Thin film deposition parameters and methodology reported in this study have been developed and consolidated according to microelectronics standards, to ensure reproducibility in the processing and reliability in the implementation, as well as thin film characteristics, including thickness homogeneity and deposition rate control, and low values of sheet resistance and roughness.

We point out that the actual amount of atomic nitrogen incorporated in the NitrAl thin films produced at variable N_2 flow values could not be reported in this work. Instead, we characterize each nitrogen concentration with the N_2 % fractional flow value used in the fabrication process.

Once the thin films are produced at wafer scale, each sample is obtained by wafer cleavage in a square geometry with approximate dimensions $7 \text{ mm} \times 7 \text{ mm}$, and fixed to a commercial chip carrier using vacuum grease where it is wire bonded with Al wires. A pair of wire bonds are placed directly on the NitrAl thin films in each of the corners of the sample to improve the electrical contact. Each sample is tested at room temperature by the Van der Pauw technique in this 4-probe configuration. The resistance of the film is obtained by fitting the resulting current-voltage (IV) curve measured with a source-meter

Table I. Range of N_2 flow values and the parameters used in the fabrication of NitrAl samples reported. The following parameters are set constant for all samples: Ar flow = 60 sccm, power set to the target $P_t = 1000$ W, nominal thickness deposition $t = 100$ nm, Ar working pressure $P_w = 5 \times 10^{-3}$ mbar, sputtering chamber base pressure $P_b = 2 \times 10^{-7}$ mbar.

N_2 (sccm)	N_2 /Ar(%)	Rate(nm/s)
0.0	0.00	1.91
1.5	2.50	1.78
2.0	3.33	1.73
3.0	5.00	1.64
4.0	6.67	1.55
5.0	8.33	1.46
6.0	10.00	1.37
7.0	11.67	1.28
8.0	13.33	1.19
9.0	15.00	1.10

instrument. To calculate the sheet resistance, we multiply the resistance obtained from the fit by the Van der Pauw constant: $\pi/\ln 2$ [43].

After the room temperature validation, each sample is mounted either on the mixing chamber stage or on the still plate of a dry dilution refrigerator with a base temperature of 20 mK. Standard magnetic shielding is employed both at room temperature and at low temperature consisting in high- μ materials. Accurate temperature control is implemented in the determination of T_c values of the thin films. As the T_c of most samples lies in the 1-3.5 K range, specific procedures to stabilize the temperature in this range are required (see Sec. A of the Supplementary Material for details).

In order to capture the entire evolution of resistance with temperature, $R(T)$, the resistance of each thin film is monitored as the system cools down/warms up. The range of swept currents is gradually adjusted to avoid excessive heat dissipation when the samples are in the normal state. Once in the superconducting state, the current is adjusted to determine the switching current value at base temperature. Then, the current range is reduced significantly below the switching current value in order to perform the T_c measurements.

Magnetic field-dependent IV-characteristics measurements of NitrAl samples are performed in a different dilution refrigerator in the KIT laboratory equipped with a vector magnet, as described in [44]. Using this experimental setup, perpendicular fields B_z up to 0.1 T and in-plane fields B_x up to 1.4 T can be applied without manually rotating the sample, while the bath temperature can be varied down to 30 mK. In this case, the approximate dimensions of the samples are reduced to 1 mm \times 3 mm to fit the special chip carrier used. The resistance values are obtained from the IV-characteristics measured in lock-in configuration about zero constant bias current I_b and 10 μ A modulation amplitude, as a function of the temperature and the magnetic field applied in the different directions. More details can be found in Sec. D1 of the Supplementary Material.

III. FUNCTIONAL CHARACTERISTICS OF THE NITRAL THIN FILMS

A. Electrical properties at room temperature

In Fig. 1(a) we show the resistivity values at room temperature ρ_{RT} for the range of thin films produced, plotted as a function of the ratio of N_2/Ar flow in the process of sputtering deposition, and for two different fabrication runs (red and black markers). The blue triangle markers represent direct determination of ρ_{RT} averaged over several points randomly chosen across the 4" wafer scale, for which dispersion is found to be about or below 3-5%. The resistivity estimations at the sample level based on the Van der Pauw technique at chip level agree with the wafer-scale averaged values.

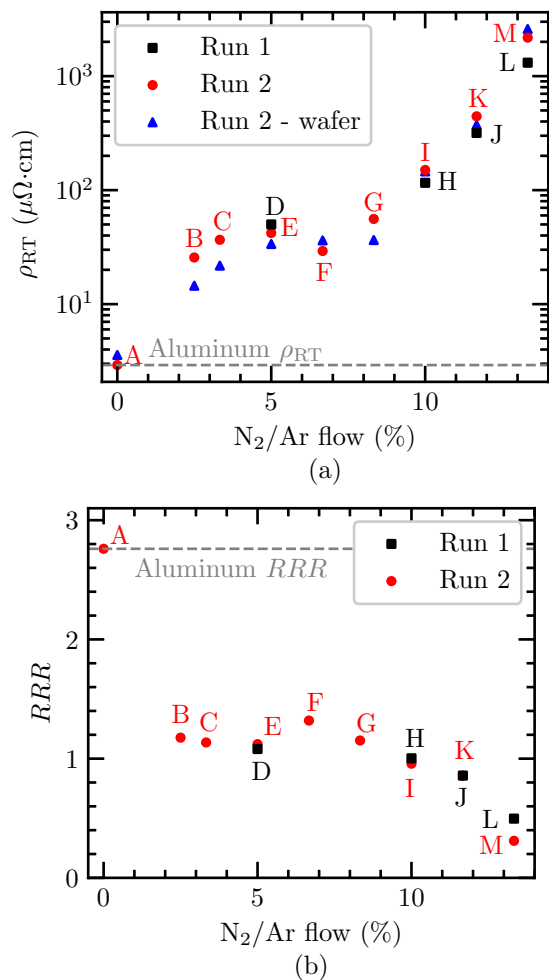


Figure 1. (a) Resistivity ρ_{RT} measured for each NitrAl film at room temperature as function of N_2 flow, relative to the fixed Ar flow used in the sputtering process. The samples labeled in black (red) were produced in the first (second) run of fabrication. The blue triangles correspond to the averaged values over a wafer scale. The Al reference values are marked with a gray dashed line for reference. (b) $RRR \equiv \rho_{RT}/\rho_{4K}$ as function of N_2 flow, ρ_{4K} being the resistivity at 4 K.

The obtained data show that the addition of N_2 flow in the sputtering process clearly impacts the thin film resistivities for all flow values, with a significant increase with respect to the 0% reference thin film (pure Al) whose value is close or nearly comparable to bulk Al. The results for the two different fabrication runs of sputtered NitrAl thin films show significant reproducibility. ρ_{RT} steadily rises up to an order of magnitude with respect to pure Al in the range 2.5%–5%. Then, between 5% and 8.33% ρ_{RT} flattens. Beyond 10%, ρ_{RT} continues to rise, following a divergent dependence, finally displaying an electrically insulating characteristic at 15% N_2 flow, with $\rho_{RT} \sim 1.5 \Omega\cdot\text{cm}$, even visible in the surface color of the sample (see Supplementary Material E for more details).

B. Electrical properties at low temperatures

In Fig. 1(b), we display the residual resistivity ratio, $RRR \equiv \rho_{RT}/\rho_{4K}$ with ρ_{4K} the resistivity measured at 4 K, as function of N_2 flow down to 4 K. The decrease in RRR as N_2 is incorporated is a clear indicator of increased disorder and impurities in the thin film [45]. Between 2.5% up to 10%, $RRR \gtrsim 1$. Above 10%, RRR tends to decrease below 1. This behaviour is reminiscent of grAl devices [46], and it is in contrast with, e.g., NbN disordered films, where the conductivity of the material gradually decreases as disorder increases [47]. Exemplary IV curves for several samples at different temperatures are shown in Fig. 6 of the Supplementary Material.

An abrupt increase of resistivity at higher N_2 flows [Fig. 1(a)] is compatible with a Superconductor-to-Insulator Transition (SIT), either driven by localization of conduction electrons (Mott) or by disorder (Anderson) [48]. The values of ρ_{RT} displayed by the NitrAl samples investigated are in the same order of magnitude as grAl devices previously reporting a Mott insulator-like phase transition [38, 46], as well as disordered NbN and NbTiN thin films displaying an Anderson-like phase transition [47, 49].

Figure 2 shows the normalized sheet resistance curves $R_s/R_{RT,s}$ obtained for different NitrAl samples in the range between 19 mK and 300 K. As the N_2 flow is increased, we observe two different regimes which we classify according to the change in slope with temperature on the different curves, as follows:

- *Metallic-like* ($dR_s/dT > 0$): In this regime the resistance monotonically decreases as temperature decreases ($RRR > 1$). For the studied set of NitrAl films, the metallic regime comprises samples produced with N_2 flows between 0% and 8.33% or, equivalently, for samples with $\rho_{RT} \lesssim 76 \mu\Omega \text{ cm}$.
- *Transition point* ($dR_s/dT \sim 0$): it is observed around the sample processed with 10% N_2 flow, which corresponds to $\rho_{RT} \sim 115\text{--}151 \mu\Omega \text{ cm}$ ($RRR \sim 1$).
- *Insulator-like* ($dR_s/dT < 0$): this regime comprises samples with increasing resistance as temperature decreases ($RRR < 1$). We include in this category samples produced with 11.67% and 13.3% of N_2 flow, or equivalently, with $\rho_{RT} \gtrsim 396 \mu\Omega \text{ cm}$. For this group of samples, we can also spot two distinctive features. For films produced with 11.67% of N_2 fractional flow, the increase in resistance is quasi-linear for decreasing temperatures. On the other hand, the most resistive samples (13.3%) show an accelerated, exponential-like increase of resistance as temperature is lowered.

Below 4 K, all NitrAl samples in the 2.5%-13.3% N_2 flow range show a normal-to-superconducting state transition at varying T_c values. Figure 3(a) shows the suppression of resistance at the transition temperature T_c

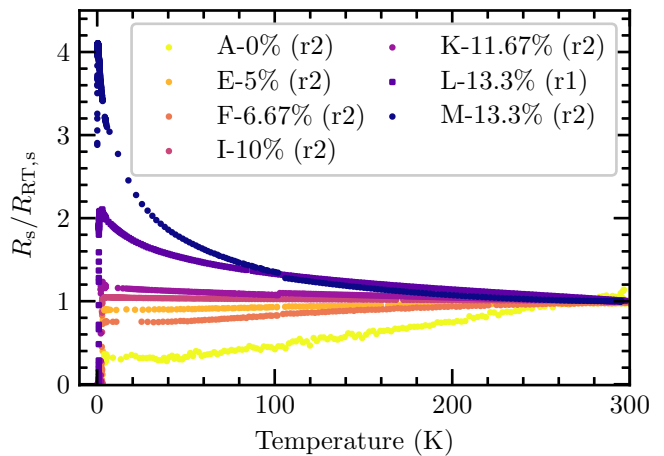


Figure 2. Normalized sheet resistance curves for several NitrAl samples. The samples with N_2 flow in the range 0% to 6.67% exhibit metallic-like behavior with $RRR > 1$. By contrast, the samples with N_2 flow in the range 11.67%-13% exhibit insulator-like behavior with $RRR < 1$. In fact, the sample 13.3% (r2) remains resistive down to the base temperature of our refrigerator (19 mK). The transition point between the two regimes appears around the sample with 10% N_2 flow with $RRR \sim 1$.

for samples with different N_2 flow fractions. We take the definition of T_c as the point where the resistance drops 50% with respect to the onset point of $R(T)$ [50]. We did not observe the superconducting transition above 19 mK for sample 13.3% produced in the second run of fabrication (r2), indicating that the SIT may lie close to that process N_2 flow value.

In several samples we have observed an increase of 20%-30% of the resistance prior to the transition to the superconducting state. Such a peak appears only for particular combination of current and voltage probes. Annex IVB 2 gives more details about this feature, which we attribute to the disordered nature of the thin films.

Figures 3(b)-(c) summarize the obtained critical temperatures as a function of N_2 flow and ρ_{RT} , respectively. Overall, the trend of T_c values changes non-monotonically, with most samples exceeding the T_c of pure Al (dashed gray-line). The highest $T_c = 3.38 \pm 0.01$ K is observed at 5% N_2 flow [51], while the 13.33% N_2 flow sample lies below Al with $T_c = 0.86 \pm 0.02$ K. The general shape of the T_c curve is dome-like, both in percentage and resistivity ρ_{RT} . However, the samples with 6.67% and 8.33% N_2 flow do not seem to evenly follow the trend of a dome. On one hand, they display a drop in T_c in the center of the dome, and, on the other hand, their values of ρ_{RT} versus T_c in Fig. 3(c) do not follow the rest of samples. A more in-depth study of NitrAl materials at the microscopic level would be required to interpret these particular features.

We note that the dome-shape of T_c versus % N_2 in Fig. 3(b) roughly defines three regions: increasing T_c (0%-5%), saturation of T_c (5%-10%) and decreasing

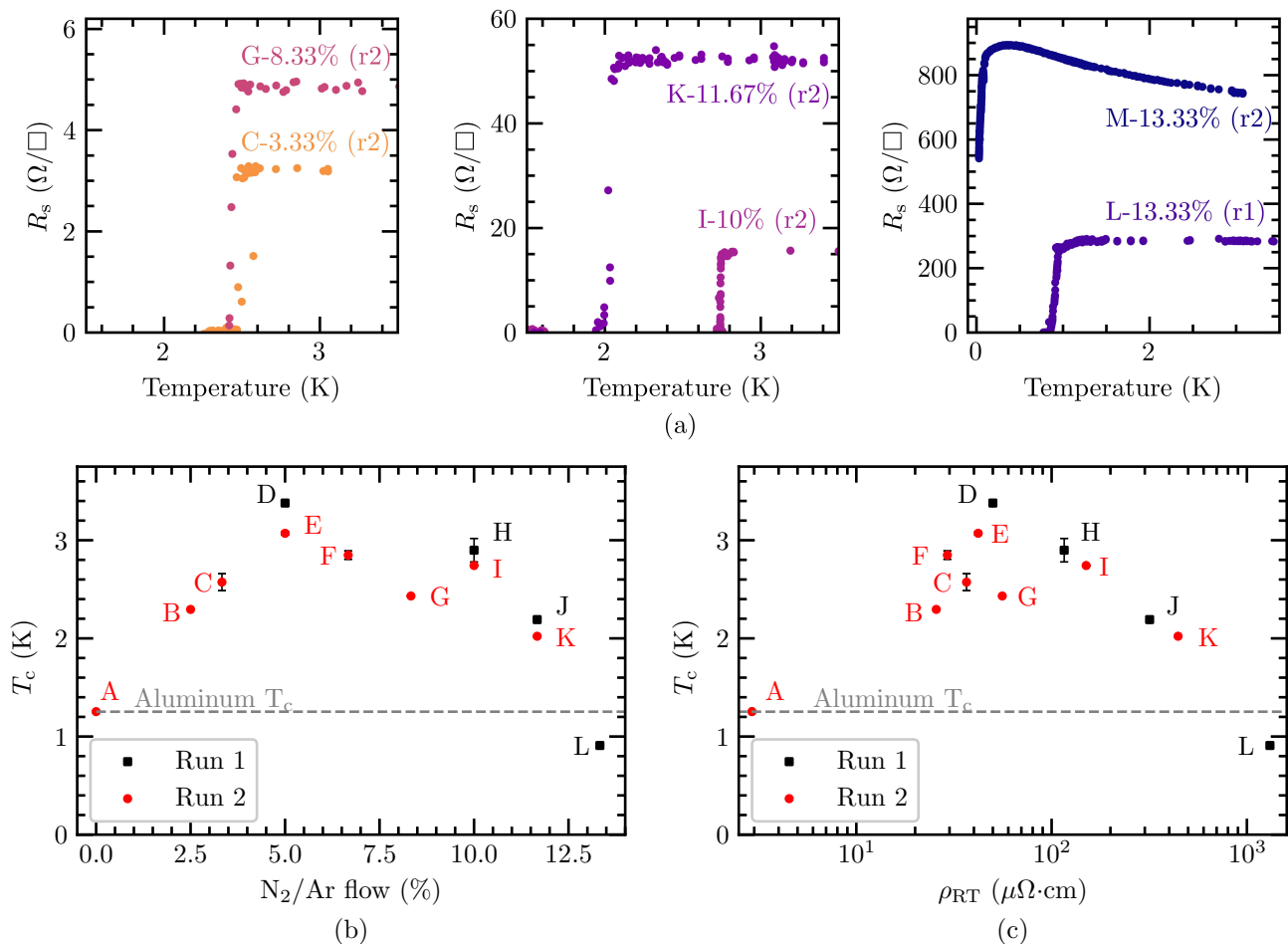


Figure 3. (a) Sheet resistance measurement near the normal metal-to-superconductor transition for different samples. Note the decrease in slope at the transition temperature for increasing N_2 flow. (b)-(c) Critical temperatures of all NitrAl samples determined by resistivity measurements as function of (b) the fraction of N_2 flow during fabrication and (c) the resistivity measured at room temperature [Fig. 1(a)]. Samples produced in the first (second) run of fabrication are shown in black squares (red circles). The T_c of aluminum (0% reference sample) is shown with a gray dashed line for reference.

T_c (10%-13.33%), which approximately correspond with the three regimes described in Fig. 1(a) of ρ_{RT} versus $\%N_2/Ar$. This correspondence points to a possible connection between ρ_{RT} and T_c driven by the same mechanism, likely the disorder and/or localization of the superconducting wave function [48]. Indeed, from the data displayed in Fig. 2, the insulator-like behavior begins at the 10% samples.

Three different regimes of T_c versus ρ have also been observed in other disordered superconductors such as grAl [52]. In the case of grAl it is argued that a competitive effect occurs with increasing concentration of oxygen between the phase stiffness J of the superconducting condensate, the charging energy E_C for a single electron to tunnel between aluminum grains, and the superconducting gap Δ [46]. In the metallic regime, a single wave function is formed by all electrons which is characterized by a phase stiffness J , orders of magnitude above E_C and Δ [that would correspond to ρ_{RT} values

below $\sim 40 \mu\Omega cm$ for our NitrAl thin films, Fig. 3(c)]. At the dome maximum, the phase stiffness J falls below the Coulomb repulsion [$\rho \sim 50 \mu\Omega cm$ in Fig. 3(c)]. At this point, the transition towards an insulator begins [48]. When $J \sim \Delta$, the Coulomb repulsion localizes the wave function in the grains and the material arrives at the SIT [$\rho > 1000 \mu\Omega cm$ in Fig. 3(c)].

This qualitative description of grAl appears to fit well to our observations with NitrAl despite that we have no evidence of the latter having a granular structure. Yet, there exist some differences. Generally, in disordered and granular superconductors the SIT is expected for resistances close to the quantum of resistance $R_Q = h/(2e)^2 \approx 6.4 k\Omega$. For the present study, the $R_{4K,s}$ threshold value for the suppression of superconductivity is $700.8 \pm 0.9 \Omega/\square$, which is almost an order of magnitude smaller than R_Q . We note that the observations of Ref. [46] are made on thinner films (20 nm thick), which likely enhance the effects by increasing the film resistance

in the normal state. For instance, we do not have evidence of features appearing at ~ 1.2 K reminiscent of pure Al for the insulating films, which might derive from the core-shell structure of grAl. The thickness-dependent effects and the microscopic material description of NitrAl will be the subject of future works, where these features will be explored explicitly in more detail.

We are in the process of building a microscopic model of NitrAl, necessary to draw quantitative conclusions from the data in Fig. 3 to understand the dominant energy scales in each range of ρ_{RT} , and to determine the type of SIT.

The values of T_c and ρ_{4K} can be used to estimate the sheet kinetic inductance ($L_{k,s}$) of the films by applying the Mattis-Bardeen formula for the complex conductivity in the local, dirty limit at low frequency ($\hbar f \ll k_B T$) and in the low temperature limit ($T \ll T_c$) [53],

$$L_{k,s} = 0.18 \frac{\hbar R_{4K,s}}{k_B T_c}, \quad (1)$$

where $R_{4K,s}$ is the normal state sheet resistance at 4 K, \hbar is the reduced Planck constant and k_B stands for the Boltzmann constant. The values of sheet kinetic inductance obtained for the NitrAl samples range between 1.31 ± 0.01 pH/ \square (0% N_2) and 422.48 ± 8.22 pH/ \square (13.3% N_2). The complete set of values for $L_{k,s}$, together with T_c , ρ_{RT} and other sample parameters, are shown in Table II. This preliminary estimation of $L_{k,s}$ points towards NitrAl as a material with high $L_{k,s}$, especially for the most resistive samples (11.67%-13.33% N_2 flow) that reach values close to other reported superinductive materials such as grAl [54].

Additionally, the critical currents I_c have been measured at base temperature for each N_2 flow value. Since these measurements were performed on thin films with no device pattern, the results only provide a qualitative understanding of the behavior of I_c in NitrAl films. The resulting values are shown in Fig. 4. Note that when the samples from both fabrication runs are sorted by ρ_{RT} (Fig. 4b) they follow an overall consistent trend, which is in contrast to the deviations between the I_c from different fabrication runs for a given N_2 flow value (Fig. 4a). For samples in the range of 8.33%-13.33% the critical current lies below that of Al, possibly indicating that the superconducting state is weakening due to the increase in disorder/localization.

C. Magnetic field response

Figure 5 shows the extracted fields at which superconductivity is destroyed B_c for perpendicular $B_{z,c}$ (a) and in-plane $B_{x,c}$ (b) externally applied magnetic fields as function of temperature.

At base temperature, the Al reference (0% N_2 flow) has a critical field below 0.01 T for B_z and 0.06 T for B_x , as expected for thin-film Al [55]. For the subset of NitrAl samples displayed in Fig. 5(a), the available range

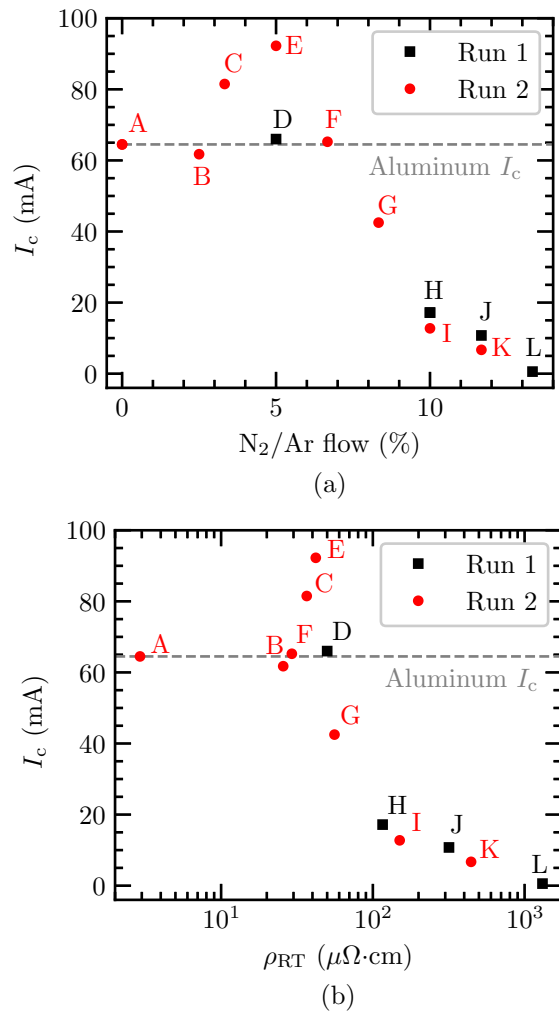


Figure 4. Critical currents I_c of NitrAl as a function of (a) the fraction of N_2 flow during fabrication and (b) the resistivity ρ_{RT} at room temperature of the samples.

of the magnet in B_z is only capable of driving the system out of the superconducting state close to the critical temperature of the NitrAl samples. On the other hand, for B_x [Fig. 5(b)] the increase of resilience of NitrAl to magnetic fields with respect to the Al reference sample is high but less pronounced. We observe an increase of almost a factor 7 in the $B_{x,c}$ for sample 3.3%. For the 10% sample, the available range of the magnet in B_x is not enough to destroy the superconducting state at base temperature.

Measurements of IV-characteristics as function of the applied magnetic fields and temperature can be found in Fig. 12 of the Supplementary Material. In particular, for the 10% sample a gradual increase of resistance is observed for the largest applied fields close to the switching current of the sample. This effect is reminiscent of type-II superconductivity where such a resistance at large applied fields close to the switching current of the sample is due to vortex flow induced by the applied current [55].

Table II. Observed parameters for the different NitrAl samples measured: sample label, N₂/Ar fractional flow (%), fabrication run number, nominal thickness t , critical temperature T_c , resistivity at room temperature ρ_{RT} , and at 4 K ρ_{4K} , estimated sheet kinetic inductance $L_{k,s}$ using Eq. (1).

Sample	N ₂ /Ar (%)	Run	t (nm)	T_c (K)	ρ_{RT} ($\mu\Omega$ cm)	ρ_{4K} ($\mu\Omega$ cm)	$L_{k,s}$ (pH/ \square)
A	0 - Al ref.	2	100.0	1.25 ± 0.01	2.92 ± 0.04	1.05 ± 0.05	0.12 ± 0.01
B	2.50	2	100.0	2.30 ± 0.01	25.66 ± 0.03	21.82 ± 0.03	1.31 ± 0.01
C	3.33	2	100.0	2.57 ± 0.08	36.67 ± 0.03	32.28 ± 0.11	1.72 ± 0.06
D	5.00	1	100.0	3.38 ± 0.01	50.01 ± 0.03	46.27 ± 0.03	1.88 ± 0.01
E	5.00	2	100.0	3.07 ± 0.02	42.07 ± 0.13	37.50 ± 0.04	1.68 ± 0.01
F	6.67	2	100.0	2.85 ± 0.04	29.25 ± 0.03	22.17 ± 0.03	1.07 ± 0.02
G	8.33	2	100.0	2.43 ± 0.01	55.88 ± 0.03	48.50 ± 0.03	2.74 ± 0.01
H	10.0	1	83.0	2.89 ± 0.12	115.97 ± 0.16	115.63 ± 0.03	6.61 ± 0.27
I	10.0	2	100.0	2.74 ± 0.01	150.26 ± 0.03	156.91 ± 0.03	7.88 ± 0.01
J	11.67	1	97.1	2.19 ± 0.01	317.52 ± 0.03	370.11 ± 0.03	23.91 ± 0.08
K	11.67	2	100.0	2.02 ± 0.01	444.13 ± 0.03	458.59 ± 0.03	35.30 ± 0.10
L	13.33	1	94.6	0.91 ± 0.02	1312.25 ± 0.03	2641.66 ± 0.05	422.48 ± 8.22
M	13.33	2	100.0	-	2177.01 ± 0.03	7008.47 ± 0.03	-

In light of this connection with type-II superconductors, the observed field at which superconductivity is destroyed may be identified as $B_c = \mu_0 H_{c2}$. Additional measurements under magnetic fields are needed to study the type of superconductivity displayed by NitrAl, but those are beyond the scope of this initial work.

The results obtained for NitrAl as function of the magnetic field follow the observations in other disordered superconductors [56, 57], where an increase in resistivity and superconducting gap with respect to the pure superconductor is accompanied by an increase in critical field.

Overall, there is a clear increase in the field at which superconductivity is destroyed in both axes B_z, B_x for increasing ρ_{RT} in the NitrAl samples. This magnetic field resilience makes NitrAl an interesting candidate to be used in circuits where high magnetic fields are required, such as, e.g., those manipulating electron spins [39] or hybrid superconductor-semiconductor structures [58]. The behaviour of NitrAl thin films under strong magnetic fields is comparable to that displayed in general by disordered superconductors, including grAl [59], NbN [47], and NbTiN [60].

IV. CONCLUSIONS

We have reported in this work an in-depth characterization of the superconducting properties of nitrized aluminum -NitrAl-, a new superconducting material that we put forward to be introduced in quantum circuits for quantum technology-related applications. By adjusting the relative concentration of nitrogen with respect to argon in the sputtering process to form the NitrAl films, we are able to control its superconducting and room temperature characteristics. For a wide parameter range, NitrAl samples display properties superior to pure Al, such as higher critical temperature (up to 3.38 ± 0.01 K) and larger fields at which superconductivity is destroyed (above 1 T for in-plane fields). The controllability of the

fabrication process, the range of reported critical temperatures and the extent of measured resistivities open the possibility to use NitrAl as a superinductor material, as well as a superconductor with adjustable T_c .

Further studies are required to infer the microscopic properties of NitrAl, particularly to discern whether the likely presence of native oxide is responsible for some of the properties observed. In addition, its behavior needs to be investigated as a material for high-frequency circuits in the form of resonators or even superconducting qubits, particularly the losses exhibited by NitrAl under these conditions.

DATA AVAILABILITY STATEMENT

Data available upon request or in the following link: <https://doi.org/10.5281/zenodo.10194875>.

ACKNOWLEDGEMENTS

The authors would like to thank Karl Jacobs from I. Physikalisches Institut, Universitaet zu Koeln, for providing the first set of NitrAl samples and for insightful discussions. We would also like to acknowledge Fabio Henriques for helping with the temperature measurements, Juan Jiménez for developing software for data analysis, and fruitful discussions with E. Driessen, T. Klapwijk, and A. Endo. We acknowledge funding from the Ministry of Economy and Competitiveness and Agencia Estatal de Investigación (RYC2019-028482-I, RYC-2016-21412, FJC2021-046443-I, PCI2019-111838-2, PID2021-122140NB-C31, PID2021-122140NB-C32, TED2021-130292B-C44), the European Commission (FET-Open AVaQus GA 899561, QuantERA), and program ‘Doctorat Industrial’ of the Agency for Management of University and Research Grants (2020 DI 41; 2020 DI 42). IFAE is partially funded by the CERCA

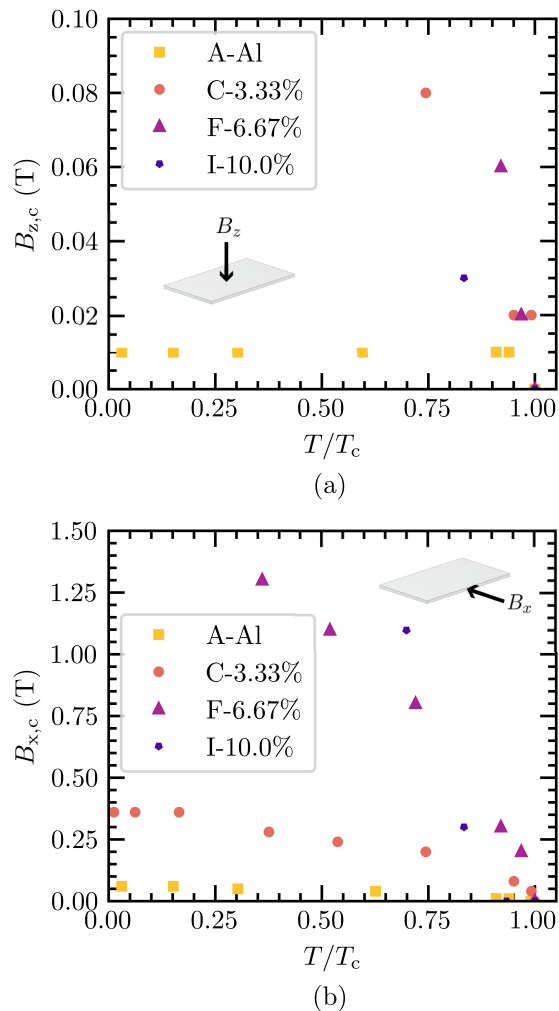


Figure 5. Magnetic fields at which superconductivity is destroyed as function of the normalized temperature in the (a) z -direction, $B_{z,c}$ (perpendicular to the chip) and (b) the x direction, $B_{x,c}$ (parallel to the chip) for different NitrAl samples produced in the second run of fabrication. The temperatures have been normalized to the critical temperature of each sample. In (a), the reference Al sample shows no temperature dependence as the smallest applicable field of 0.01 T already drives it in the normal state at base temperature.

program of the Generalitat de Catalunya. This study was supported by MICIIN with funding from European Union NextGenerationEU(PRTR-C17.I1) and by Generalitat de Catalunya.

-
- [1] Blais A, Grimsom A L, Girvin S M and Wallraff A 2021 *Rev. Mod. Phys.* **93**(2) 025005
- [2] Pérez-Salinas A, López-Núñez D, García-Sáez A, Forn-Díaz P and Latorre J I 2021 *Phys. Rev. A* **104**(1) 012405
- [3] Martinis J M, Cooper K B, McDermott R, Steffen M, Ansmann M, Osborn K D, Cicak K, Oh S, Pappas D P, Simmonds R W and Yu C C 2005 *Physical Review Letters* **95** 210503
- [4] Siddiqi I 2021 *Nature Reviews Materials* **6** 875–891
- [5] Bruno A, de Lange G, Asaad S, van der Enden K L, Langford N K and DiCarlo L 2015 *Applied Physics Letters* **106** ISSN 0003-6951 182601
- [6] Gurevich A 2023 *Superconductor Science and Technology* **36** 063002
- [7] Wang C, Axline C, Gao Y Y, Brecht T, Chu Y, Frunzio L, Devoret M and Schoelkopf R J 2015 *Applied Physics Letters* **107** 162601
- [8] Leduc H G, Bumble B, Day P K, Eom B H, Gao J, Gollwala S, Mazin B A, McHugh S, Merrill A, Moore D C et al. 2010 *Applied Physics Letters* **97** 102509
- [9] Vissers M R, Gao J, Wisbey D S, Hite D A, Tsuei C C, Corcoles A D, Steffen M and Pappas D P 2010 *Applied Physics Letters* **97** 232509

- [10] Chang J B, Vissers M R, Córcoles A D, Sandberg M, Gao J, Abraham D W, Chow J M, Gambetta J M, Beth Rothwell M, Keefe G A et al. 2013 Applied Physics Letters **103** 012602
- [11] Bretz-Sullivan T M, Lewis R M, Lima-Sharma A L, Lidsky D, Smyth C M, Harris C T, Venuti M, Eley S and Lu T M 2022 Applied Physics Letters **121**
- [12] Mutsenik E, Linzen S, Il'ichev E, Schmelz M, Ziegler M, Ripka V, Steinbach B, Oelsner G, Hübner U and Stolz R 2023 Low Temperature Physics **49** 92–92
- [13] Frasca S, Arabadzhiev I, de Puechredon S B, Oppliger F, Jouanny V, Musio R, Scigliuzzo M, Minganti F, Scarlino P and Charbon E 2023 Physical Review Applied **20** 044021
- [14] de Graaf S E, Adamyan A A, Lindström T, Erts D, Kubatkin S E, Tzalenchuk A Y and Danilov A V 2017 Phys. Rev. Lett. **118**(5) 057703
- [15] de Graaf S E, Faoro L, Burnett J, Adamyan A A, Tzalenchuk A Y, Kubatkin S E, Lindström T and Danilov A V 2018 Nature Communications **9** 1143
- [16] Barends R, Vercruyssen N, Endo A, De Visser P, Zijlstra T, Klapwijk T and Baselmans J 2010 Applied Physics Letters **97** 033507
- [17] Coumou P C J J, Zuiddam M R, Driessen E F C, de Visser P J, Baselmans J J A and Klapwijk T M 2013 IEEE Transactions on Applied Superconductivity **23** 7500404–7500404
- [18] Gyenis A, Mundada P S, Di Paolo A, Hazard T M, You X, Schuster D I, Koch J, Blais A and Houck A A 2021 PRX Quantum **2**(1) 010339
- [19] Dorenbos S N, Reiger E M, Perinetti U, Zwiller V, Zijlstra T and Klapwijk T M 2008 Applied Physics Letters **93** 131101 ISSN 0003-6951
- [20] Dorenbos S N, Forn-Díaz P, Fuse T, Verbruggen A H, Zijlstra T, Klapwijk T M and Zwiller V 2011 Applied Physics Letters **98** 251102 ISSN 0003-6951
- [21] Mantegazzini F, Ahrens F, Borghesi M, Falferi P, Fasolo L, Faverzani M, Ferri E, Labranca D, Margesin B, Mezzena R et al. 2023 Physica Scripta
- [22] Zhao S, Withington S and Thomas C N 2023 arXiv preprint arXiv:2306.00685
- [23] Niepce D, Burnett J and Bylander J 2019 Physical Review Applied **11** 044014
- [24] Levy-Bertrand F, Benoît A, Bourrion O, Calvo M, Catalano A, Goupy J, Valenti F, Maleeva N, Grünhaupt L, Pop I and Monfardini A 2021 Phys. Rev. Appl. **15**(4) 044002
- [25] Coiffard G, Daal M, Zobrist N, Swimmer N, Steiger S, Bumble B and Mazin B A 2020 Superconductor Science and Technology **33** 07LT02
- [26] Harris E 1974 Applied Physics Letters **24** 514–516
- [27] Morgan J S 1990 Properties of sputtered thin films of indium nitride and aluminum nitride (The Johns Hopkins University)
- [28] Cleland A N, Pophristic M and Ferguson I 2001 Applied Physics Letters **79** 2070–2072
- [29] Shu L, Peng B, Li C, Gong D, Yang Z, Liu X and Zhang W 2016 Sensors **16** 526
- [30] Chou M H, Dumur E, Zhong Y P, Peairs G A, Bienfait A, Chang H S, Conner C R, Grebel J, Povey R G, Satzinger K J and Cleland A N 2020 Applied Physics Letters **117** ISSN 0003-6951
- [31] Kim S, Terai H, Yamashita T, Qiu W, Fuse T, Yoshihara F, Ashhab S, Inomata K and Semba K 2021 Communications Materials **2** 98
- [32] Nakamura Y, Terai H, Inomata K, Yamamoto T, Qiu W and Wang Z 2011 Applied Physics Letters **99** 212502
- [33] Zijlstra T, Lodewijk C F J, Vercruyssen N, Tichelaar F D, Loudkov D N and Klapwijk T M 2007 Applied Physics Letters **91** ISSN 0003-6951 233102
- [34] Abeles B, Cohen R W and Cullen G W 1966 Phys. Rev. Lett. **17**(12) 632–634
- [35] Grünhaupt L, Spiecker M, Gusenkova D, Maleeva N, Skacel S T, Takmakov I, Valenti F, Winkel P, Rotzinger H, Wernsdorfer W, Ustinov A V and Pop I M 2019 Nature Materials **18** 816–819
- [36] Valenti F, Henriques F, Catelani G, Maleeva N, Grünhaupt L, von Lüpke U, Skacel S T, Winkel P, Bilmes A, Ustinov A V, Goupy J, Calvo M, Benoît A, Levy-Bertrand F, Monfardini A and Pop I M 2019 Phys. Rev. Appl. **11**(5) 054087
- [37] Cohen R W and Abeles B 1968 Phys. Rev. **168**(2) 444–450
- [38] Grünhaupt L, Maleeva N, Skacel S T, Calvo M, Levy-Bertrand F, Ustinov A V, Rotzinger H, Monfardini A, Catelani G and Pop I M 2018 Phys. Rev. Lett. **121**(11) 117001
- [39] Samkharadze N, Zheng G, Kalhor N, Brousse D, Sammak A, Mendes U C, Blais A, Scappucci G and Vandersypen L M K 2018 Science **359** 1123–1127
- [40] Gül Ö, Zhang H, Bommer J D, de Moor M W, Car D, Plissard S R, Bakkers E P, Geresdi A, Watanabe K, Taniguchi T et al. 2018 Nature nanotechnology **13** 192–197
- [41] The properties of the silicon wafers used for this study are the following. Type/dopant: p/Bor; resistivity: 4–40 Ω cm; orientation: $\langle 100 \rangle \pm 1^\circ$; diameter: 100.0 \pm 0.3 mm; thickness: 525 \pm 15 μ m; single sided polished; primary flat: $\langle 101 \rangle \pm 1^\circ$, 32.5 \pm 2.5 mm.
- [42] Vissers M R, Gao J, Kline J S, Sandberg M, Weides M P, Wisbey D S and Pappas D P 2013 Thin Solid Films **548** 485–488 ISSN 0040-6090
- [43] van der Pauw L J 1958 Philips technical review **20** 220–224
- [44] Thirion C, Wernsdorfer W, Jamet M, Dupuis V, Mélinon P, Pérez A and Maily D 2002 Journal of magnetism and magnetic materials **242** 993–995
- [45] Fickett F 1971 Cryogenics **11** 349–367 ISSN 0011-2275
- [46] Levy-Bertrand F, Klein T, Grenet T, Dupré O, Benoît A, Bideaud A, Bourrion O, Calvo M, Catalano A, Gomez A et al. 2019 Physical Review B **99** 094506
- [47] Chand M, Saraswat G, Kamlapure A, Mondal M, Kumar S, Jesudasan J, Bagwe V, Benfatto L, Tripathi V and Raychaudhuri P 2012 Phys. Rev. B **85**(1) 014508
- [48] Gantmakher V F and Dolgoplov V T 2010 Physics-Uspexhi **53** 1
- [49] Driessen E F C, Coumou P C J J, Tromp R R, de Visser P J and Klapwijk T M 2012 Phys. Rev. Lett. **109**(10) 107003
- [50] Poole C, Farach H, Creswick R and Prozorov R 2014 Superconductivity Elsevier insights (Elsevier Science) ISBN 9780124166103
- [51] It is likely that and even higher T_c than the one observed at 5% lies in a N_2 flow not sampled by the discrete set of values used in this work.
- [52] Dynes R C and Garno J P 1981 Phys. Rev. Lett. **46**(2) 137–140

- [53] Rotzinger H, Skacel S T, Pfirmann M, Voss J N, Münzberg J, Probst S, Bushev P, Weides M P, Ustinov A V and Mooij J E 2016 Superconductor Science and Technology **30** 025002
- [54] Maleeva N, Grünhaupt L, Klein T, Levy-Bertrand F, Dupre O, Calvo M, Valenti F, Winkel P, Friedrich F, Wernsdorfer W et al. 2018 Nature communications **9** 3889
- [55] Tinkham M 2004 Introduction to superconductivity (Courier Corporation)
- [56] Bachar N, Lerer S, Levy A, Hacoheh-Gourgy S, Almog B, Saadaoui H, Salman Z, Morenzoni E and Deutscher G 2015 Phys. Rev. B **91**(4) 041123
- [57] Abeles B, Cohen R W and Stowell W R 1967 Phys. Rev. Lett. **18**(21) 902–905
- [58] Kringhøj A, Larsen T W, Erlandsson O, Uilhoorn W, Kroll J, Hesselberg M, McNeil R, Krogstrup P, Casparis L, Marcus C and Petersson K 2021 Phys. Rev. Appl. **15**(5) 054001
- [59] Borisov K, Rieger D, Winkel P, Henriques F, Valenti F, Ionita A, Wessbecher M, Spiecker M, Gusenkova D, Pop I M and Wernsdorfer W 2020 Applied Physics Letters **117** 120502
- [60] Müller M, Luschmann T, Faltermeier A, Weichselbaumer S, Koch L, Huber G B, Schumacher H W, Ubbelohde N, Reifert D, Scheller T et al. 2022 Materials for Quantum Technology **2** 015002
- [61] Poláčková M, Zhitlukhina E, Belogolovskii M, Gregor M, Plecenik T and Seidel P 2023 The European Physical Journal Plus **138** 1–8
- [62] Vaglio R, Attanasio C, Maritato L and Ruosi A 1993 Physical Review B **47** 15302
- [63] Hake R 1967 Physical Review **158** 356

SUPPLEMENTARY MATERIAL

A. IV current characteristics

The dilution refrigerator is in a stable configuration with the pulse tube ON while the 4K, Still, and mixing chamber (MXC) plates are thermally connected. No 3He/4He mixture is circulating. A small quantity (20-50 mbar) of mixture (total ~ 500 mbar) is introduced in the system. When all plates are at the same temperature, the MXC and Still plates are thermally isolated, while the Still remains in thermal contact with the 4K plate. In this configuration, the MXC can be stabilized using its heater to temperatures below the ones reachable by only employing the pulse tube (3-4K). If the Still is then isolated from the 4K plate and more mixture is condensed in a controlled way, the system can slowly reach temperatures ~ 1 K or lower. The temperature of the mixing chamber and the Still can be modified by using their individual heaters and/or by restoring the thermal connection between the two plates. The whole procedure can be sped up or slowed down by controlling the amount of mixture in circulation and the heat introduced by the Still and MXC heaters.

Figure 6 shows different IV current characteristics for different NitrAl samples. The figure is a zoom into the range used for the low temperature T_c measurements. There is a recurring offset in the voltage axis related to the source-meter setup.

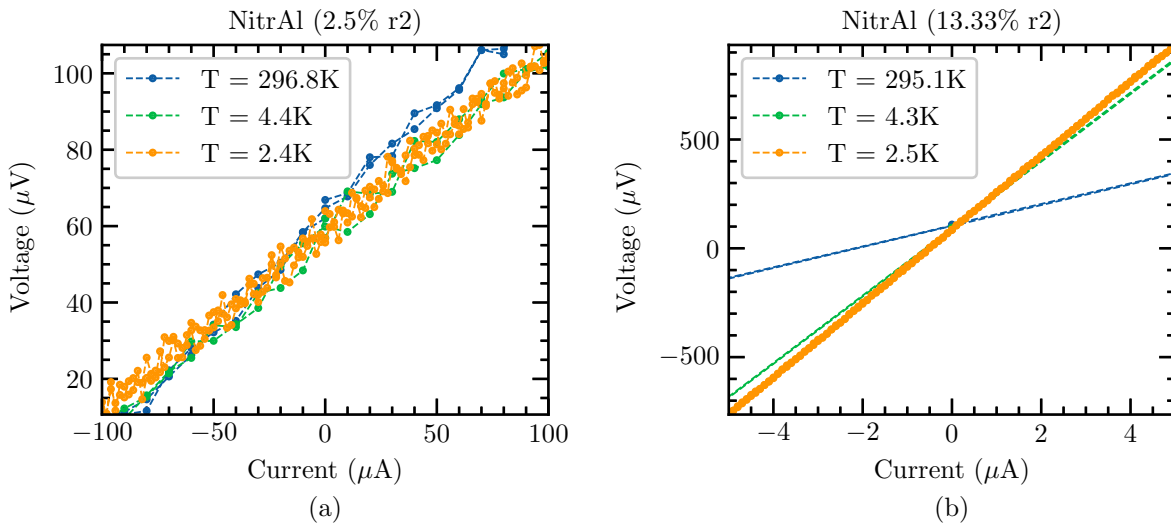


Figure 6. Current-Voltage (IV) characteristics for sample with 2.5% N_2 (a), and 13.3% N_2 (b). Notice the difference in voltage ranges used for both samples.

B. Resistance curves

1. Normalized resistance curves

In Figure 7 we provide the normalized sheet resistance curves not shown in the main text.

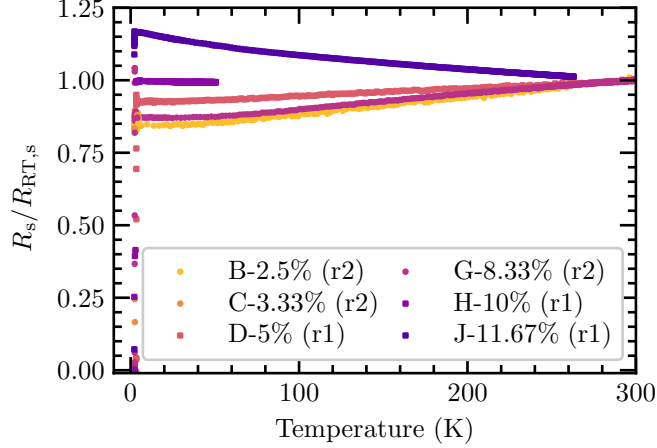


Figure 7. Normalized sheet resistance curves for several NitrAl samples.

2. Resistance peak near the superconducting transition

In several samples we have observed an increase of 20%-30% of the resistance prior to the transition to the superconducting state. Such a peak appears only for the combination of current and voltage probes giving slightly higher resistance. We tested different probe configurations (see Figure 8) for two samples near the superconducting transition. In Figure 9 we plot the resistance versus temperature for different probe configurations labeled as CA, CB, CC following the nomenclature of Figure 8. We did not include the in-line configuration C for sample G-8.33% due to the low resistance and noise in the measurement.

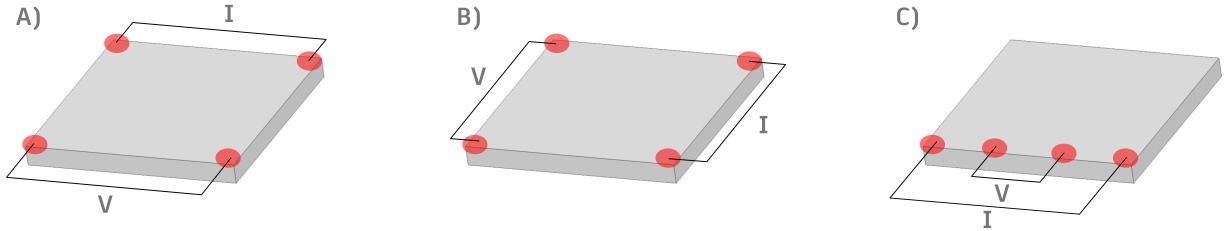


Figure 8. Different contact locations for the four probe configuration used to test the origin of the anomalous peak near the superconducting transition.

With the first configuration (A) we measured slightly larger resistances and we observed the spike before the superconducting transition. Rotating the contacts (B) provided slightly lower resistance and we were not able to reproduce the rapid increase in the $R(T)$ curve near T_c . Finally, with the in-line configuration (C), no spike was visible. A similar phenomenon has been observed in other disordered and homogeneous thin films measured in 4-probe configuration [61, 62]. The anomalous peak can be attributed to local variations of T_c and current redistribution effects on the sample. Actually, the critical temperatures measured in different 4-probe configurations differ slightly by 0.01K.

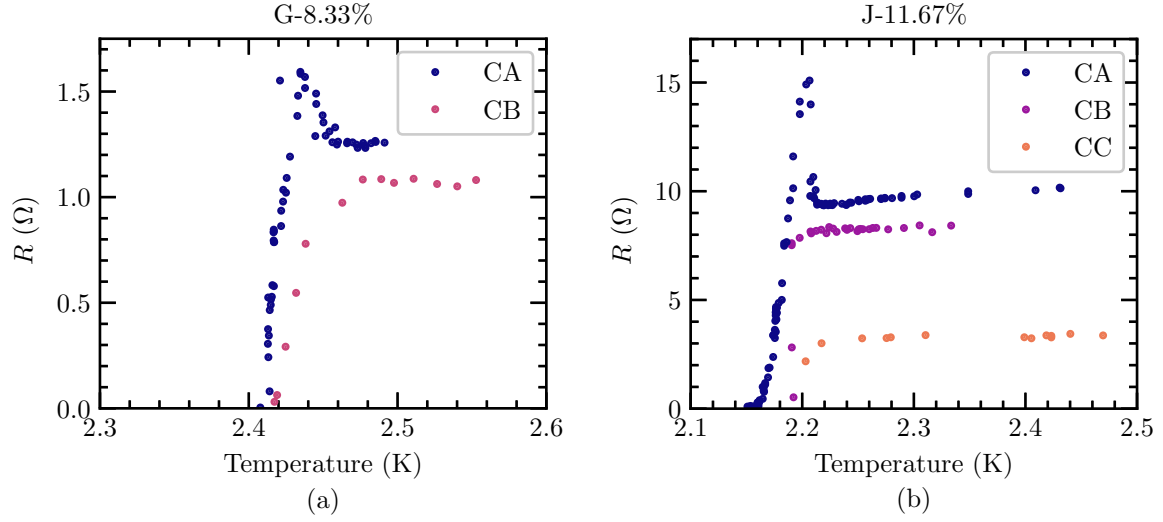


Figure 9. Resistance versus temperature for NitrAl (a) 8.33% in two different 4-probe configurations and (b) 11.67% in three different 4-probe configurations.

C. Sheet kinetic inductance and London penetration depth

Using Eq. (1), in Fig. 10 we plot the resulting sheet kinetic inductance as function of (a) the N_2 flow and (b) as function of the room temperature resistivity.

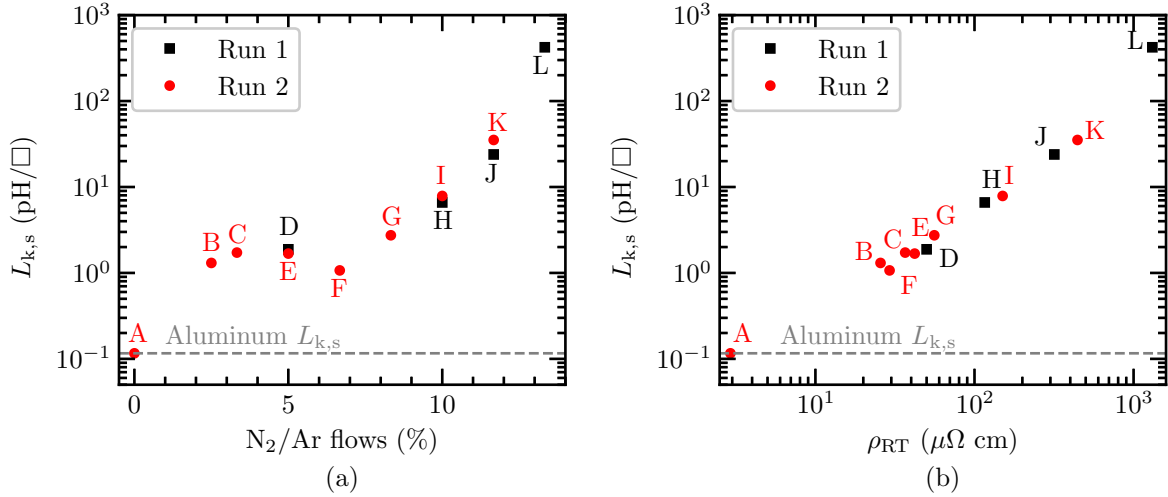


Figure 10. Estimated sheet kinetic inductance using Eq. (1) for different N_2 flow values (a), and as function of room temperature resistivity ρ (b).

Figure 10(a) shows a similar trend as ρ at room temperature, with an initial jump with respect to pure Al, an intermediate regime with constant values, and a final exponential increase above 10%.

Similarly, in Figure 11 we plot the London penetration depth estimated using the following expression [63],

$$\lambda_L \simeq 105 \text{ nm} \sqrt{\frac{\rho_{4K} (\mu\Omega \text{ cm})}{T_c (\text{K})}}. \quad (2)$$

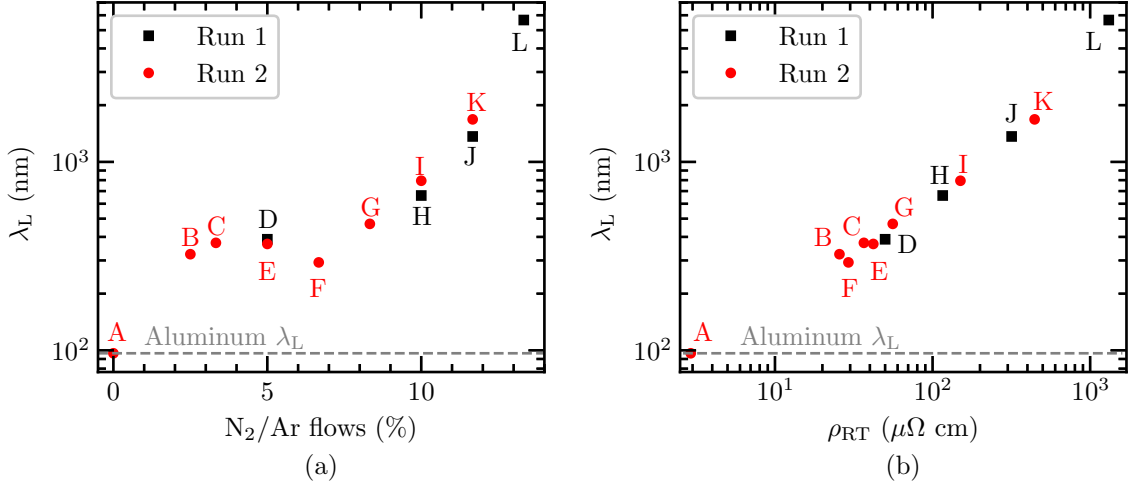


Figure 11. London penetration depth estimated for different NitrAl samples as a function of (a) N_2 flow values, and (b) room temperature resistivity ρ .

D. Magnetic field measurements

1. Experimental setup

The samples are connected to the I-V measurement setup by wire bonding, in a simple four probe arrangement. An ADWIN gold data acquisition system and NanoQt interface was used to acquire amplified voltage data as well as apply bias voltage through a high resistor to obtain a bias current through the NitrAl thin-film samples. Such a simple configuration works as a constant current source, since the NitrAl film resistances used in these measurements at room temperature are very small ($< 30 \Omega$) compared to the high-resistance bias resistor ($R_b = 10 \text{ k}\Omega$). The maximum bias current I_b was limited to 1 mA by the maximum voltage V_b range of $\pm 10 \text{ V}$ from the ADWIN output. A Femto commercial voltage amplifier was used to with a gain 100/ 1000/ 10000 depending on the magnitude of the small voltage at the sample.

In addition to the direct I-V measurements, dV/dI at each bias current were measured by an integrated lock-in code in the ADWIN interfaced with NanoQt. A small oscillating bias current modulation of amplitude $10 \mu\text{A}$ and frequency 91 Hz was added about each I_b to measure sample resistance (dV/dI) in the lock-in configuration. The in-phase and 90 degree phase shifted components of this oscillating signal were used as a reference to measure the in-phase and out of phase components of the response voltage, which were filtered by a fourth order filter with time constant set to 50 ms (about 5 oscillations at signal frequency). The squared sum of these in-phase and out of phase components provides R^2 . The bias current I_b was varied very slowly such that during a lock-in data acquisition, the I_b change can be ignored. The dV/dI obtained from lock-in measurement and from the slope of direct I-V data were compared to find that both methods provide similar results. However, the lock-in measurements show less noise, hence the resistance measured only in lock-in configuration are presented.

2. IV-characteristics under magnetic field

As a complement to the data shown in Sec. IV of the main text, we show here raw data of the IV-characteristics. Note that the maximum current of the source employed is 1 mA.

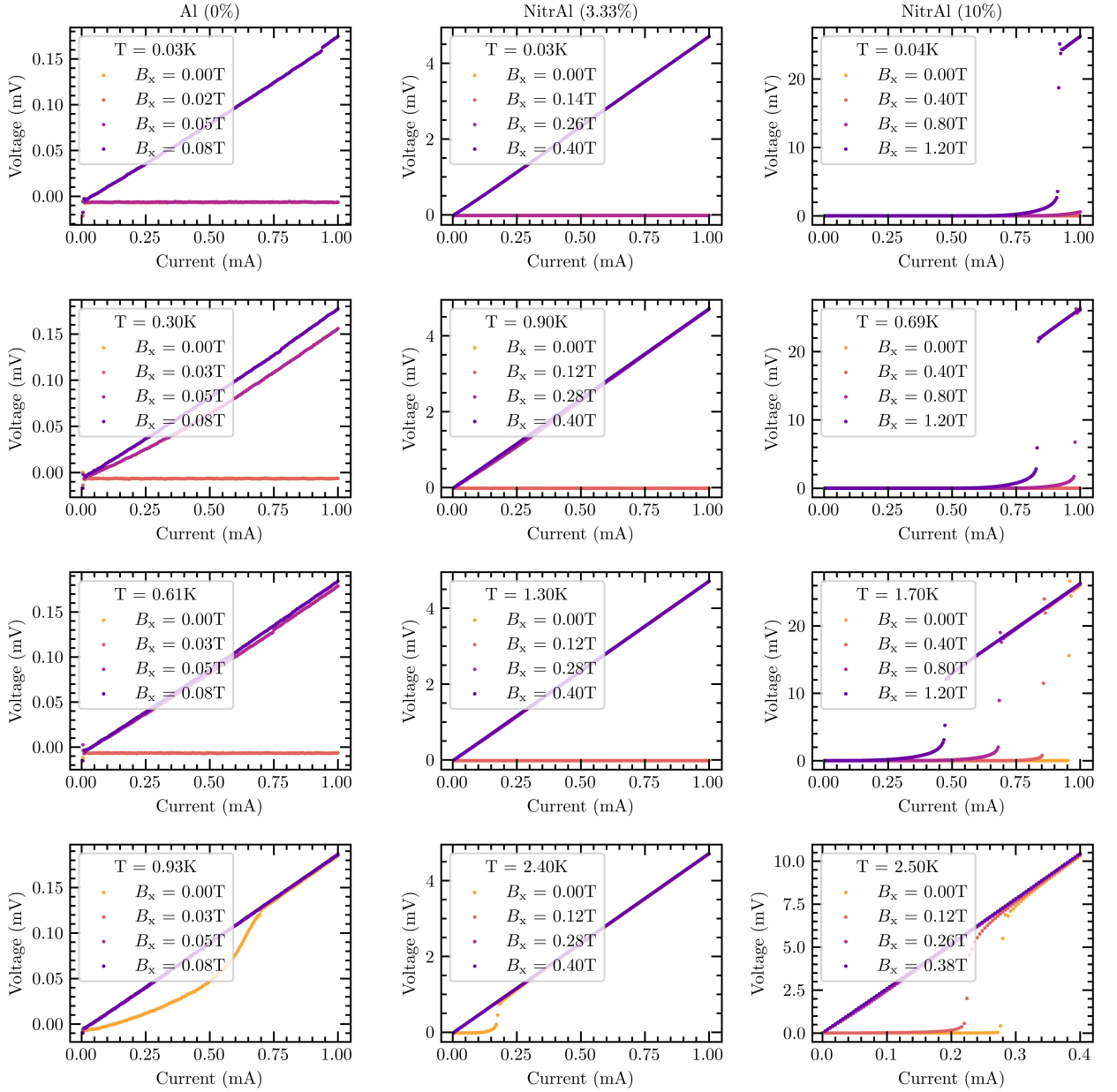


Figure 12. VI-characteristics as a function of the temperature and the magnetic field in the x -direction, B_x (in-plane with the chip) for different NitrAl samples produced in the second run of fabrication.

E. Optical properties

We can also connect the resistivity at room temperature with the surface appearance of the samples (Fig. 13). A qualitative difference in the surface color of the films is observed between conductive and insulating samples. These differences might indicate a change in the optical properties and optical responses of the films. In particular, for conducting samples the surface is shiny and silver-looking, close to the one of aluminum, while samples above 13.3% appear to be silver-green. A quantitative analysis of the optical response of the thin films at room temperature will be included in a future work.

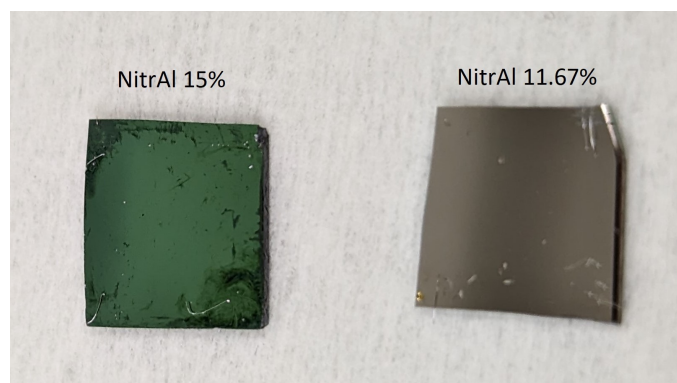


Figure 13. NitrAl films produced with different N_2/Ar flows. A clear difference in color between the insulating sample (15%), of dark green, and the conductive one (11.67%), of dark gray, can be observed.